Surface & Coatings Technology 446 (2022) 128789

Contents lists available at ScienceDirect

Surface & Coatings Technology

journal homepage: www.elsevier.com/locate/surfcoat

Electrochemical, mechanical, and tribological properties of corrosion product scales formed on X65 steel under CO_2 supercritical pressure environments

Katryanne Rohana Georg Bacca, Natália Feijó Lopes, Giovanni dos Santos Batista, Carlos Alexandre dos Santos, Eleani Maria da Costa *

School of Technology, Pontifical Catholic University of Rio Grande do Sul, 6681 Ipiranga Avenue, Building 30, Room 111/F, 90619-900 Porto Alegre, RS, Brazil

ARTICLE INFO

Keywords:
API 5 L X65 steel
CO_2-corrosion
Scales
Supercritical CO_2
$FeCO_3$
$Fe_xCa_{1-x}CO_3$

ABSTRACT

This study investigates the properties of corrosion product scales formed on API 5 L X65 steel under CO_2 supercritical pressure for 7 and 15 days in NaCl solution and brine. The structure, composition, electrochemical performance, mechanical, and tribological properties of the scales were characterized using multiple techniques, including scanning electron and atomic force microscopies, X-ray microtomography, X-ray diffraction, potentiodynamic polarization, electrochemical impedance spectroscopy, nanoindentation, and wear tests. The $FeCO_3$ scales exhibited superior properties to $Fe_xCa_{1-x}CO_3$. The presence of Ca^{2+} in brine favored scale dissolution, decreased the protection capability of steel against CO_2-corrosion, and deteriorated the mechanical properties and wear resistance.

1. Introduction

The costs related to corrosion are very high. In 2016, the global corrosion cost was estimated to be US$ 2.5 trillion according to the NACE report [1], excluding individual safety or environmental consequences. A similar situation prevails in the oil and gas industry, where the direct and indirect costs of corrosion are extremely high [2,3]. Low-carbon and microalloyed carbon steels have frequently been used for oil and gas production operations as well as CO_2 transport, capture, and storage systems (CCS, carbon capture and storage). The widespread use of these types of steels can be attributed to their higher availability and low cost compared to those of other high-alloyed steels. However, microalloyed steels such as API X65 steel have relatively low corrosion resistances. If corrosion is not properly controlled, it can cause enormous economic impact and environmental damage owing to corrosion failures [3–6]. A common type of corrosion in the steels used in oil fields is CO_2-corrosion, which can occur in the presence of other corrosive agents [3,7,8]. The CO_2-corrosion mechanism is composed of transport, chemical, and electrochemical processes, which occur between steel and aqueous CO_2, as dry CO_2 is not corrosive at the temperatures at which oil production systems operate [3,8,9]. Important reserves of oil and gas, such as pre-salt reservoirs, are particularly challenging owing to the presence of severe conditions for materials, including high pressure, high temperature, and high CO_2 content, which present a risk of severe corrosion. The operations involved in injecting CO_2 for CCS purposes are critical in many aspects, such as the transport and storage of CO_2 occur above supercritical pressure (CO_2 critical point is 7.38 MPa and 31.1 °C), and long-term material integrity is required.

Numerous studies have shown that the properties of corrosion product scales formed on steel surfaces play an important role in CO_2-corrosion. When the corrosion product scales are compact, dense, and adherent to the steel surface, the CO_2-corrosion rate can be significantly reduced over [10–12]. However, the processes involved in the formation of scales are complex, and how each environmental variable affects the composition and properties of scales is not fully understood. The main corrosion product formed in presence of CO_2 and water and absence of oxygen is iron carbonate ($FeCO_3$). The scales can contain two layers: an inner layer consisting of Fe_3C (cementite), due to preferential corrosion of ferrite and $FeCO_3$, and an outer layer composed only of $FeCO_3$. Cementite can act as a cathodic site because it is conductive, which can lead to galvanic pair formation with ferrite, thereby accelerating corrosion [13,14]. In addition, the presence of Ca^{2+} and Mg^{2+}, among other cations, in aqueous solutions affects the scale composition, forming mixed carbonates, thus influencing the protective properties of the

* Corresponding author.
E-mail address: eleani@pucrs.br (E.M. Costa).

https://doi.org/10.1016/j.surfcoat.2022.128789
Received 17 June 2022; Received in revised form 4 August 2022; Accepted 5 August 2022
Available online 17 August 2022

scales [10,15–18]. However, there is still no consensus on the effect of these ions on protective properties. Some studies have observed an increase in corrosion rates [15,18], whereas others have found that mixed carbonate scales are more protective [16,19]. The higher the temperature, the lower the corrosion rate of steel, indicating that temperature has an important effect on the protective capacity exerted by scale in steel [16,20]. This indicates that under CO_2 transport conditions, for example, where temperatures are typically lower, scales can offer less protection to steel. The CO_2 pressure also has a determining effect on the scale properties, and in general, the higher the pressure, the greater the protection conferred [16,21–24]. However, most of these investigations were performed at low pressures (<1 MPa). Furthermore, the evaluation of the scale electrochemical properties is also of fundamental importance in elucidating the formation mechanism because it can act as a barrier for ion migration to reach the substrate and to determine the changes in protective characteristics with corrosion time. Nevertheless, studies on the electrochemical protection properties of corrosion product growth in CO_2 supercritical environments using precorroded steel specimens are scarce [22]. The mechanical and wear properties of the scales are also important factors in protecting steel, especially when high fluid flow rates are present, which can lead to physical removal of the corrosion products, or when steels are in relative motion between the contacting components. However, relatively few studies have evaluated the mechanical properties of corrosion product scales, their relationship with the composition, and their effect on the corrosion rate [20,24,25]. In addition, investigations on the tribological properties of formed scales and their influence on substrate protection are rare [26,27].

As discussed above, scales can provide different degrees of protection to steel depending on the kinetics of formation, morphology, microstructure, and chemical composition, among other properties. Therefore, these scales can influence both the corrosion rate and the corrosion mechanism [16]. Most of the existing studies have investigated the composition and microstructure of scales as a function of environmental variables, but there are few studies that address their electrochemical performance, and mechanical and tribological properties, especially for those formed under high CO_2 pressure. In addition, the studies evaluated the scale properties using steels of different chemical compositions and microstructures under different environmental variables and different experimental procedures for corrosion tests, making it extremely difficult to compare them. In this context, this study aims to conduct a comprehensive and systematic study for assessing the structural, electrochemical, mechanical, and tribological properties of corrosion products formed on API X65 steel at CO_2 high pressure in the presence of NaCl or brine to better understand the effect of corrosion product properties on CO_2-corrosion. Multiple characterization techniques were used as mass loss measurements, scanning electron microscopy (SEM), atomic force microscopy (AFM), X-ray diffraction (XRD), potentiodynamic polarization (PP), electrochemical impedance spectroscopy (EIS), X-ray microtomography (X-ray MCT), nanoindentation, and fretting wear tests. The fretting wear test is a powerful technique widely used to evaluate coating properties; however, to the best of our knowledge, this technique has not yet been applied to determine the wear properties of CO_2-corrosion products scales.

2. Experimental procedures

2.1. Preparation of steel specimens

The API 5L X65 steel investigated in this study is widely used in pipelines in the oil and gas sectors. Table 1 shows the chemical composition of the steel obtained using optical emission spectroscopy (OES), and the values are average of five measurements. The steel specimens were extracted from a hot rolled steel welded pipe. The hardness value of the as-received material is 91 ± 2 HRB. The X65 steel microstructure is shown in Fig. 1, which is composed of ferrite (light phase) and a small amount of pearlite (lamellae microconstituent), showing a typical microstructure of low carbon steels. The microstructure also contains fine and dispersed carbides precipitated along the grain boundaries. All specimens were analyzed in the as-received condition, without heat treatment.

For the corrosion tests, the X65 prismatic specimens were ground with SiC papers up to #1200 grit, polished with alumina of sizes 1 and 0.3 μm, consecutively, washed with distilled water, cleaned with acetone in an ultrasonic bath for 5 min, and subsequently weighted using a 0.0001 g precision balance. In total, six prismatic specimens with different dimensions were used with each corrosion test condition for the various characterization techniques.

2.2. Corrosion procedures to obtain the scales

Corrosion parameters were chosen to represent conditions similar to those encountered during oil-field operations. The corrosion experiments were performed in a 600 mL AISI 316 stainless steel Parr pressure vessel at a temperature of 40 ± 1 °C and a pressure of 15 MPa for periods of 7 d and 15 d; Fig. 2 illustrates the experimental setup. Corrosion was evaluated in two different media: in 3.5 % NaCl, which is approximately the salinity found in seawater, and in brine that simulates Brazilian pre-salt formation water. The chemical composition of brine is listed in Table 2.

Prior to the experiments, the solutions were deoxygenated by bubbling N_2 and CO_2 (99.9 % purity supplied by Air Products) for 2 h each, and then the system was pressurized with CO_2 until a pressure of 15 MPa was reached. After removal from the reactor, the specimens were washed in distilled water and acetone, dried in hot air, and

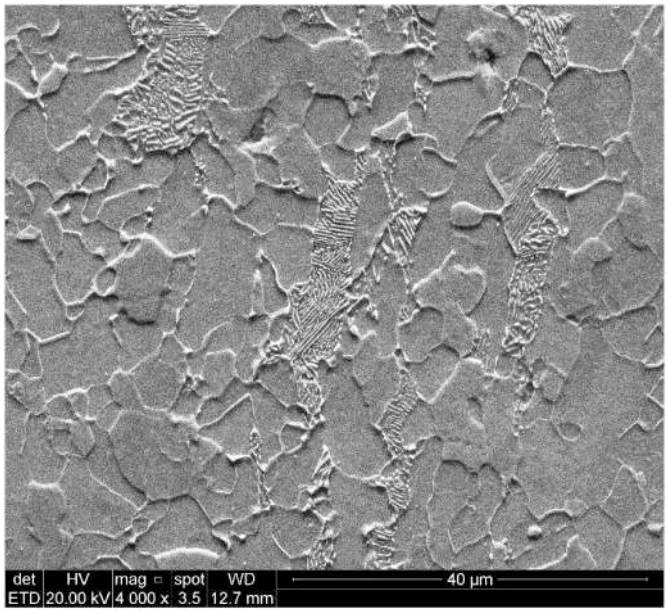

Fig. 1. SEM image of the API5L X65 steel microstructure.

Table 1
Chemical composition of the API X65 steel (wt%).

C	Si	Mn	P	S	Cr	V	Nb	Ni	B	Cu	Ti	Fe
0.122	0.260	1.440	0.019	0.003	0.030	0.035	0.040	0.020	0.005	0.016	0.035	Balance

Fig. 2. Schematic arrangement for corrosion experiments in Parr pressure vessel. 1) Heating blanket; 2) Pressure vessel; 3) Specimen holder; 4) Specimens; 5) Temperature controller.

Table 2
Chemical composition of the brine prepared with 200 mL Mili-Q water.

Salt reagent grade	Mass (g)	Ion	Concentration (mg/L)
NaCl	5.782	Na^+	11,400
KCl	0.168	K^+	442
$CaCl_2.2H_2O$	0.054	Ca^{2+}	74
$MgCl_2.6H_2O$	0.120	Mg^{2+}	72
Total chloride	–	Cl^-	18,280

maintained in a vacuum desiccator for further characterization of the corrosion product scales.

2.3. Characterization of corrosion product scales

After corrosion induction, the corrosion product scales were characterized by multiple techniques, including SEM, XRD, AFM, X-ray MCT, PP, EIS, nanoindentation, and fretting wear tests. In addition, the chemical compositions of the solutions were analyzed before and after corrosion. The mass-loss tests were performed to obtain the general corrosion rate.

2.3.1. Surface analysis

The SEM was used to obtain information about the microstructure, morphology, homogeneity, and thickness of the scales; images were obtained with a field emission scanning electron microscope (FE-SEM, Inspect F50-FEI) using the secondary electron mode. The measurements of scale thickness were performed in 15 different locations on the specimen by using low magnification (200×) SEM images and Image J software [28]. The elementary composition of the scale was determined using energy dispersive X-ray spectroscopy (EDS) with an Oxford Instruments detector.

The AFM was used to analyze the morphology and roughness of the scales. A Bruker Dimension Icon TP atomic force microscope with a cantilever of nominal thickness 6.25 μm, resonance frequency 525 kHz, and spring constant 200 N/m was used. The limitation of height measurement (z axis) of the AFM topography analysis provided by the equipment is about 20 μm, which is higher than the roughness of scales (<10 μm). The scanned area was 50 × 50 μm.

The XRD analyses were performed using a Bruker diffractometer (D8 ADVANCE) with a Cu source (Cu kα1 radiation) under the conditions of 40 kV and 30 mA. The angle was varied from 2θ = 10–80° with a step size of 0.015° over a duration of 0.03 s.

Microtomography images were acquired using a Bruker microtomograph (microCT SkyScan1173) under the conditions of 130 kV, 61 mA, and 7 μm resolution, to compare the density of scales depending on the medium and corrosion time. Specimens with dimensions of approximately 7.5 × 4 × 5 mm were scanned before and after corrosion for determining the volume changes due to corrosion.

2.3.2. Solution analysis

The chemical composition (cation concentration) of the solution was analyzed before and after the corrosion tests using an inductively coupled plasma spectrometer (ICP-OES, Perkin Elmer, Optima 7000 DV). The measurement was repeated three times for each sample.

2.3.3. Electrochemical measurements

The PP and EIS analyses were used to evaluate the capability of the scales to protect the steel substrate against corrosion and the mechanisms involved. Electrochemical measurements were performed using a classical three-electrode cell connected to a potentiostat (Autolab PGSTAT 302 N model). The electrochemical cell comprised a platinum wire counter electrode (CE), saturated calomel reference electrode (SCE), and API X65 precorroded steel as the working electrode (WE). All electrochemical measurements were performed in duplicate in a 0.1 M Na_2SO_4 electrolyte under aerated conditions. This electrolyte was chosen because it is a strong ionic electrolyte and offers low corrosivity level to steel with low tendency to promote localized attack allowing better evaluation of the scale properties as barrier for ion migration towards to steel substrate. The main chemical reaction involves the iron dissolution to forms iron sulfate [29]. All potentials were referenced to the SCE (E = 241 mV vs. NHE). Prior to each electrochemical measurement, the WE was immersed in the electrolyte for 1 h to attain steady-state open-circuit potential (OCP). The EIS analysis was performed in a frequency range of 10,000–0.1 Hz and an amplitude of ±10 mV. The PP measurements were performed in the voltage range of −300 mV to +300 mV corresponding to the value for the OCP with a scan rate of 1 mV/s. Autolab Nova 2.1® software was used to analyze the electrochemical data from the PP curves by the Tafel extrapolation method. The EIS data were correlated to different circuit elements to choose the one that best represents the properties of the scales. The electrical parameters were obtained by fitting the EIS data using ZView® software.

2.3.4. Mechanical properties

The mechanical properties (hardness and elastic modulus) of the scales were determined by an instrumented hardness test (IHT), also known as nanoindentation, using Fischerscope HV100 equipment. The measurements were performed at different points on the scale. Each load–discharge cycle was configured with a total time interval of 80 s (40 s for loading and 40 s for unloading) to ensure proper contact between the Knoop indenter and specimen. The maximum applied load was 100 mN. A holding stage of 10 s at peak load was used to minimize creep effects [30], and each test was repeated at least five times. The load was applied on the scale surface and maximum penetration depth caused by the indenter into the scale was 1.8 μm which is <10 % of the total scale thickness. Hardness values were calculated according to the ISO 14577 standard. The elastic modulus (*E*) of the corrosion product scales was measured based on the unloading–displacement curve during nanoindentation, and was obtained using Eq. (1).

$$E = \frac{\sqrt{\pi}}{2^*\sqrt{A_c}} \times S \tag{1}$$

where A_c is the contact area (m^2), and S is the contact stiffness (N/m).

Dry fretting wear tests were performed according to the ASTM G133 standard test method using a linear high-frequency reciprocating rig tribometer and a ball-on-flat plane geometry (HFRR 2 model, Ducom). The tests were carried out using hardened AISI 52100 chrome steel balls (6 mm diameter, 62–63 HRC hardness) as the counter body with 1 mm stroke length at a frequency of 10 Hz, 53 % relative humidity, and 25 °C. Two normal loads (2 N and 8 N) were used to determine the wear behavior of both the outer (superficial) and inner (sub-superficial) scale layers. Tests were performed for two durations (10 and 30 min), and tests were performed in duplicate for each condition. The coefficient of friction (COF) and wear rate (W) were analyzed for each test. The kinetic COF, defined as the ratio between the tangential and normal forces during the test, was obtained directly using the HFRR software, and the wear rate was calculated using Eq. (2):

$$W = \frac{V}{D} \tag{2}$$

where W is given in (mm^3/m), D is the sliding distance (mm) and V is the wear material removal volume (mm^3).

The sliding distance (m) was calculated using Eq. (3):

$$D = 0.002 \times t \times f \times L \tag{3}$$

where f is the frequency (Hz - cycles/s), t is the total test time (s), and L is the stroke length (mm).

The wear removal volume was calculated using Eq. (3), considering that the wear scar has a semi-ellipsoid geometry:

$$V = \frac{12}{\pi} \times B \times C^2 \tag{4}$$

where B is the major-axis length of the ellipsoid and $C = A$ are the minor-axis lengths, which were measured using an optical microscope (OM) with a 0.01 mm resolution. The wear scar surfaces were analyzed using SEM.

2.3.5. Mass loss tests

Mass loss tests to obtain the general corrosion rates were conducted according to the ASTM G1-03 standard test method [31] in precorroded prismatic specimens with dimensions of approximately 15 × 10 × 8.5 mm. For this purpose, the solution was prepared using HCl and distilled water at a 1:1 ratio with the addition of hexamethylenetetramine (3.5 g/L). The scale of each specimen was removed from the steel surface by

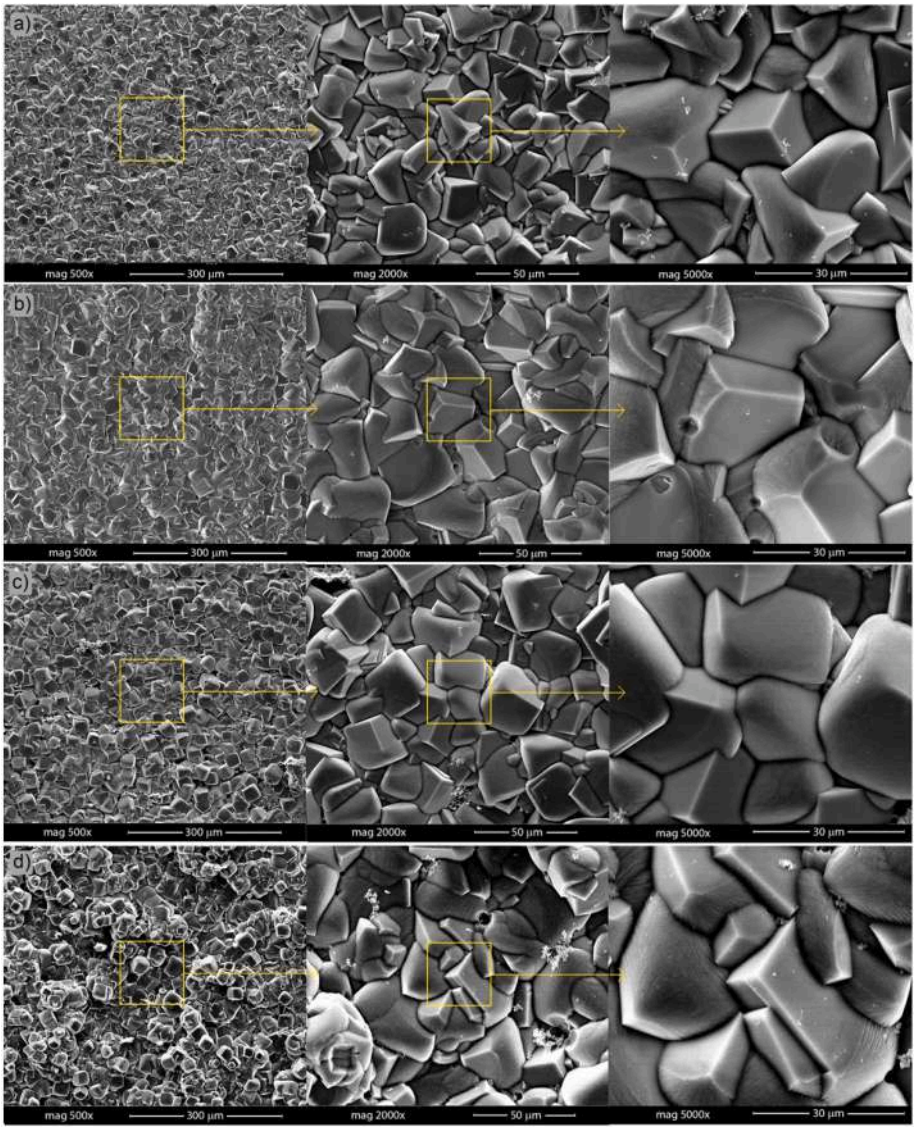

Fig. 3. SEM images for morphology of scales growth on X65 steel surface at 40 °C and 15 MPa in different media and times: a) 7 d/brine; b) 15 d/brine; c) 7 d/NaCl; and d) 15 d/NaCl.

immersion in the acid solution for 30 s at room temperature, rinsed with distilled water and acetone, dried in hot air, and weighed using a 0.0001 g precision balance. This procedure was repeated for 20 cycles until constant mass loss was observed, and the tests were performed in duplicate. The general corrosion rate (GCR) in mm/y was determined using Eq. (5).

$$GCR = \frac{K \times \Delta w}{A \times t \times p} \quad (5)$$

were K is a constant ($K = 8.76 \times 10^4$ in mm/y) [31], Δw is weight loss (g), A is the surface area of specimen (cm^2), t is the duration of exposure (h), and ρ is density of steel (g/cm^3).

3. Results and discussions

3.1. Morphology and thickness of the scales

The morphologies of the scales formed in the brine and NaCl solutions after 7 d and 15 d are presented in Fig. 3. The steel surface was completely covered with prismatic carbonate crystals under all experimental conditions. Although at atmospheric pressure and 40 °C the formation of $FeCO_3$ is not favorable at pH 3 [32], the formation of $FeCO_3$ at high pressure occurs, as also observed by other authors [11,23,33]. The size of the crystals in brine was slightly smaller than that in NaCl solution, particularly for the short period of corrosion (7 d), indicating that other cations present in brine, such as Ca^{2+}, can accelerate the precipitation of carbonate.

From the cross-sectional images of the scales (Fig. 4), voids are observed in the scales formed in brine and NaCl after 7 d at the interface with steel. These voids can act as diffusion channels, thereby promoting further metal dissolution. After 15 d, the scales are more compact and thinner than those after 7 d. At the beginning of CO_2-corrosion process the corrosion rate is expected to be high because cementite (Fe_3C) and ferrite form a galvanic couple. Ferrite is preferentially dissolved due to its higher energy and electric potential [14]. This is the reason that cementite is surrounded by corrosion product near the steel surface, as shown in Fig. 4. The precipitation of $FeCO_3$ is initiated when the concentrations of Fe^{2+} and CO_3^{2-} species exceed the solubility limit. The relationship between $FeCO_3$ crystal growth and nucleation has important influence on scale properties. The formation of porous scale, at the beginning of corrosion process (Fig. 4a and b), is related to low nucleation rate which induces a large space between the iron carbonate crystals that allows solution to permeate through scale. As the CO_2-corrosion is a dynamic process, the corrosion rate changes during the entire corrosion process, and consequently the $FeCO_3$ nucleation and growth rates are altered. With the progressing of corrosion process over time, the corrosion rate decreases because the scale becomes denser (Fig. 4 b and d), acting as a more effective barrier against the diffusion of corrosive species. The scales formed during 15 d in both environments, NaCl solution and brine, are slightly thinner and more uniform than those formed during 7 d. This is related to pores filling with carbonates and scale densification and compaction over time under high pressure. These effects were also reported in other studies [11,12,24]. The scale thickness formed in brine has an average of 58.1 ± 4.6 μm and in NaCl solution 71.3 ± 8.6 μm after 7 d, and the thicknesses decreased after 15d to 50.5 ± 4.5 μm and 49.6 ± 4.3 μm, respectively. These values were obtained measuring 15 different locations along the scale transversal section.

The 3D AFM images of the scale morphology are presented in Fig. 5. The roughness information is provided in Table 3, where the values are presented in terms of quadratic roughness (R_q), average roughness (R_a), and maximum roughness (R_{max}). There was a decrease in the scale roughness from 7 d to 15 d for both brine and NaCl solutions, and the

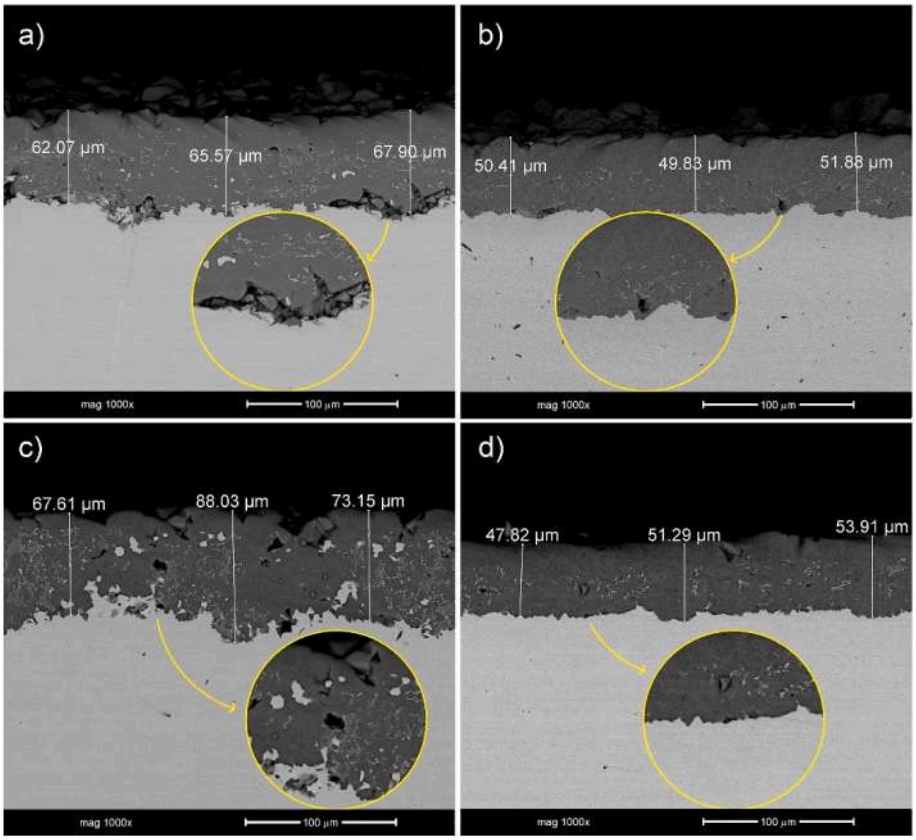

Fig. 4. SEM images for cross sections of the corrosion product scales formed on X65 steel surface at 40 °C and 15 MPa in different media and times: a) 7 d/brine; b) 15 d/brine; c) 7 d/NaCl; and d) 15 d/NaCl.

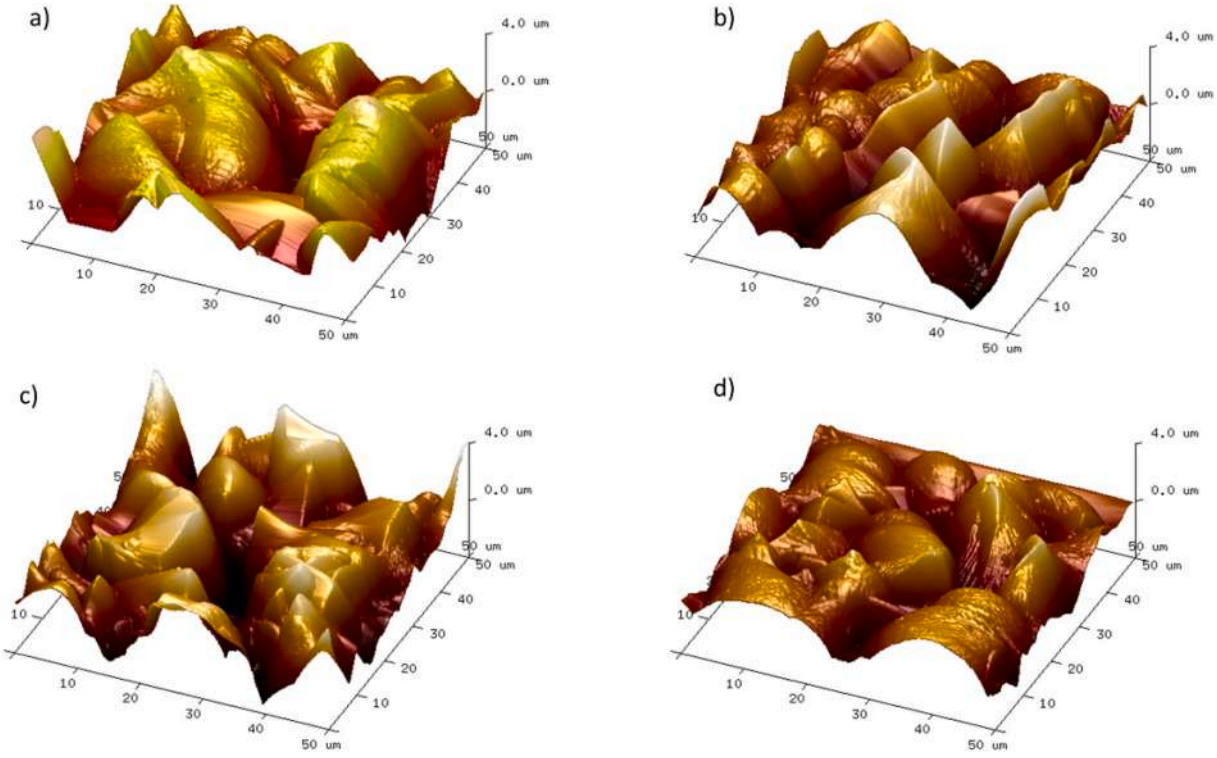

Fig. 5. 3D AFM images of morphology of scale growth on X65 steel surface at 40 °C and 15 MPa in different media and times: a) 7 d/brine; b) 15 d/brine; c) 7 d/NaCl; and d) 15 d/NaCl.

Table 3
Roughness of corrosion product scales obtained by AFM.

Conditions	R_q (nm)	R_a (nm)	R_{max} (nm)
7 d Brine	1163 ± 16	905 ± 52	8342 ± 319
15 d Brine	972 ± 198	773 ± 151	7299 ± 1705
7 d NaCl	1379 ± 92	1073 ± 83	10,014 ± 327
15 d NaCl	1013 ± 149	805 ± 116	7088 ± 1608

scales grown in NaCl solution were slightly less rough than those grown in brine after 15 d. These results are according with SEM images (Fig. 4) observed, which have shown regular compactness and thickness with corrosion process increasing.

3.2. Chemical composition and structure of the scales

All scales had a two-layer structure (inner and outer layers), as shown in Fig. 6. The inner layer was composed of carbides and carbonates owing to the preferential dissolution of ferrite, and the outer layer was composed only of carbonates. As the interface between inner and outer layer is not well-defined, the layers boundaries in Fig. 6 were delineated considering the presence or not of carbides. After 15 d of corrosion, the outer layer was thicker than that after 7 d.

The X-ray MCT analysis of the specimens after corrosion is presented in Fig. 7, which shows color differential contrast images based on the density difference between the steel substrate and scale. Fig. 7 also shows the scale cross-section density maps built using Quickgrid software® from X-ray MCT data. Close to the steel surface, the inner layer exhibited a densely packed structure (yellow color), which was more uniformly distributed in the specimens corroded for 15 d in the NaCl solution. In general, the outer layer has a lower density (green color) than the inner layer (yellow color), possibly associated with coarser carbonate crystals. As the specimens were scanned before and after corrosion by X-ray MCT, it was possible to estimate total volume variation of each specimen, and the calculated values are shown in Fig. 7. All specimens increased in volume owing to the formation of corrosion product scale, since the scale density is lower than the steel density. The specimens corroded in brine exhibited a higher volume increase.

The SEM images and respective EDS line scan analysis of scales are presented in Fig. 8, which shows the presence of Ca and Mg, in addition to Fe, C, and O, in the composition of the scale grown in brine. The result indicates that this scale is composed of complex carbonates, whereas that formed in NaCl is composed only of $FeCO_3$. Complex mixed carbonates have been reported in many studies on CO2-corrosion in the presence of brine [10,15,17,18,25].

Table 4 shows the quantification of cations (Fe^{2+}, Ca^{2+}, K^+, and Mg^{2+}) in the solutions before and after corrosion. The Fe^{2+} concentration was higher after 7 d of corrosion in both the brine and NaCl solutions because there is a greater accumulation of Fe^{2+} in the solution owing to the higher corrosion rate, as shown further in the mass loss results. The lower Fe^{2+} content after 15 d can be attributed to the precipitation of iron carbonates on the steel surface. However, considering the standard deviation, the average K^+ and Mg^{2+} contents in the solution remained almost the same. Thus, the contents of these elements in the corrosion scales are probably very low, as their presence was detected in the EDS analysis. Nevertheless, the Ca^{2+} concentrations in the brine decreased in the solution after the corrosion induction tests for both 7 d and 15 d, indicating that the Ca^{2+} from the brine migrated to the metal surface, forming a mixed carbonate scale $Fe_xCa_{1-x}CO_3$. These results agree with the EDS and XRD analyses. The stoichiometric composition of $Fe_xCa_{1-x}CO_3$ varied with the corrosion time. The scales became enriched with Ca with increasing corrosion time, as revealed by the brine composition after corrosion (Table 4). As expected, the consumption of Ca^{2+} from the brine was approximately twice as high during 15 d of corrosion as 7 d, as shown in Table 4.

The XRD patterns of the scales (Fig. 9) corroborate that the scales grown in NaCl solution contain $FeCO_3$, while those in brine are composed of mixed carbonate ($Fe_xCa_{1-x}CO_3$). The presence of Ca in the

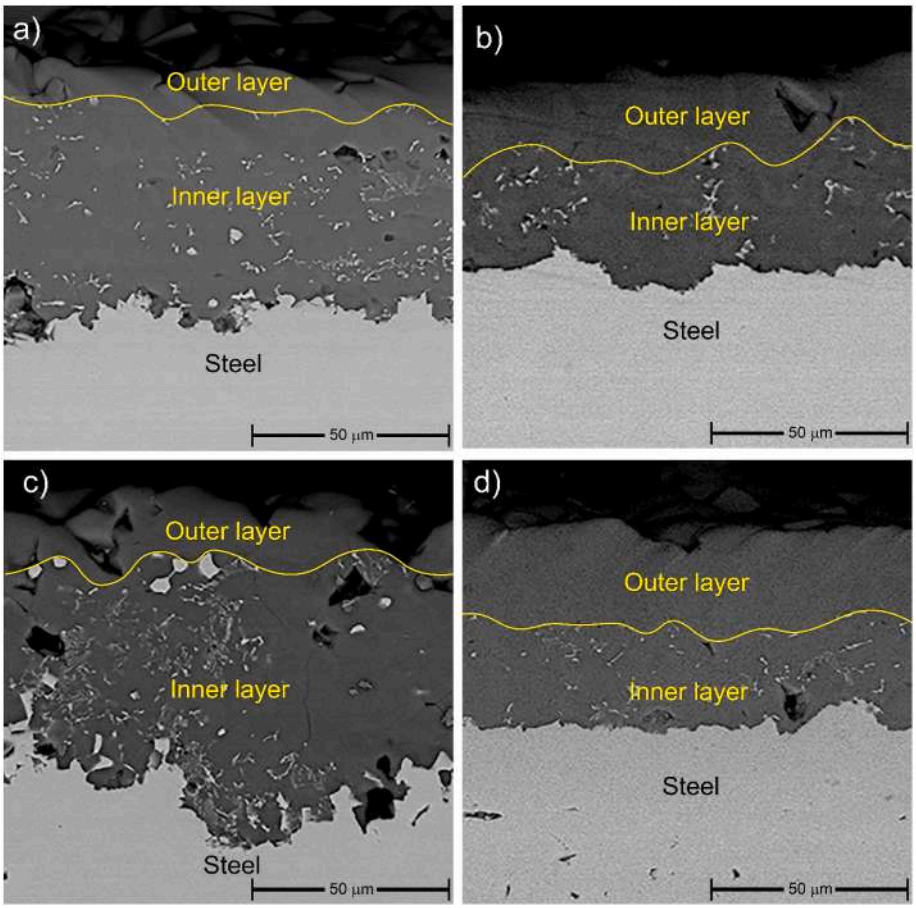

Fig. 6. SEM images of cross sections of the corrosion product scales illustrating the formation of double layer a) 7 d/brine; b) 15 d/brine; c) 7 d/NaCl; and d) 15 d/NaCl.

scale grown in brine promotes small shifts to lower angles in the characteristic peaks of $FeCO_3$ because the replacement of Fe by Ca atoms in the $FeCO_3$ unit cell causes an increase in the interplanar spacing, as previously reported [10,17]. Although the SEM images in Fig. 6 clearly show the presence of carbides in the inner layer, the characteristic peaks of this compound were not detected in the XRD analysis.

3.3. Electrochemical performance of the scales

Fig. 10 shows the scale polarization curves compared with X65 steel in 0.1 M Na_2SO_4, and Table 5 presents the electrochemical parameters obtained by the Tafel method. All the scales have provided corrosion protection. However, the scales formed in the NaCl solution presented a slightly less active corrosion potential (E_{corr}) when compared with scales formed in brine for pre-corrosion times of 7 d and 15 d. Furthermore, the scales constituted for 15 d conferred more protection to the substrate than 7 d, once the scales formed in 15 d have presented lower corrosion potential (E_{corr}), lower current density (i_{corr}), and higher polarization resistance (R_p). After a longer corrosion time (15 d), the $FeCO_3$ scale formed in NaCl provided more protection to the steel substrate than that by $Fe_xCa_{1-x}CO_3$ formed in brine. This observation agreed with previous studies [10,11,15,17,18,25].

Fig. 11 shows the Nyquist and Bode plots of the corrosion product scales in 0.1 M Na_2SO_4 obtained using EIS. Different electric circuit elements were tested. The electrical equivalent circuit (EEC) chosen to better represent the double-layer scale and that provide the best fitting are also presented (Fig. 11e). The electrochemical parameters obtained from the equivalent circuit fitting for all scales are shown in Table 6.

The Nyquist plots show similarity in the protective mechanisms owing to the presence of a single capacitive arc in the high-frequency region and a linear tail in the low-frequency region (Warburg impedance) related to diffusion-controlled ion transport. The capacitive arc in the high-frequency range can be attributed to charge transfer associated with the effect of the electric double-layer capacitance. The electrochemical impedance shows that the protective characteristic is inferior in case of scales growth for 7 d (Fig. 11a and c) than those for 15 d (Fig. 11b and d), which is consistent with the PP results (Fig. 10 and Table 5). The amplitude of the capacitive semicircle increases in scales formed at 15 d (Fig. 11b), which can be related to the increase in the protective characteristic of the scale with increasing immersion time in a CO_2-corrosive environment. However, the smaller capacitive semicircle exhibited by scales formed in brine at 15 d may indicate a higher dissolution of $Fe_{1-x}Ca_xCO_3$, which allows ion migration through the pores of the scale. In the low-frequency region, the phase angle of the scales initially increases and then gradually decreases. This aspect also indicates that the corrosion resistance initially increases and then weakens owing to electrolyte permeation through the existing pores. The capacitive arcs were squashed, which is possibly associated with surface inhomogeneity. The EIS results showed that the $FeCO_3$ scales offered a stronger barrier to the mass transfer of corrosive species.

The EEC of the impedance that best fits the scales corresponds to a substrate coated with two overlaid porous layers (Fig. 11e). This EEC is characterized by a double-layer capacitance (CPE_{dl}) and a Faradaic process denoted by the charge transfer resistance (R_{ct}), connected in series with the additional resistances of the solution inside the pores of the outer and inner layers (R_{outer} and R_{inner}), respectively. The two capacitors related to the inner and outer layers are represented by constant phase elements CPE_{outer} and CPE_{inner}, respectively, because the

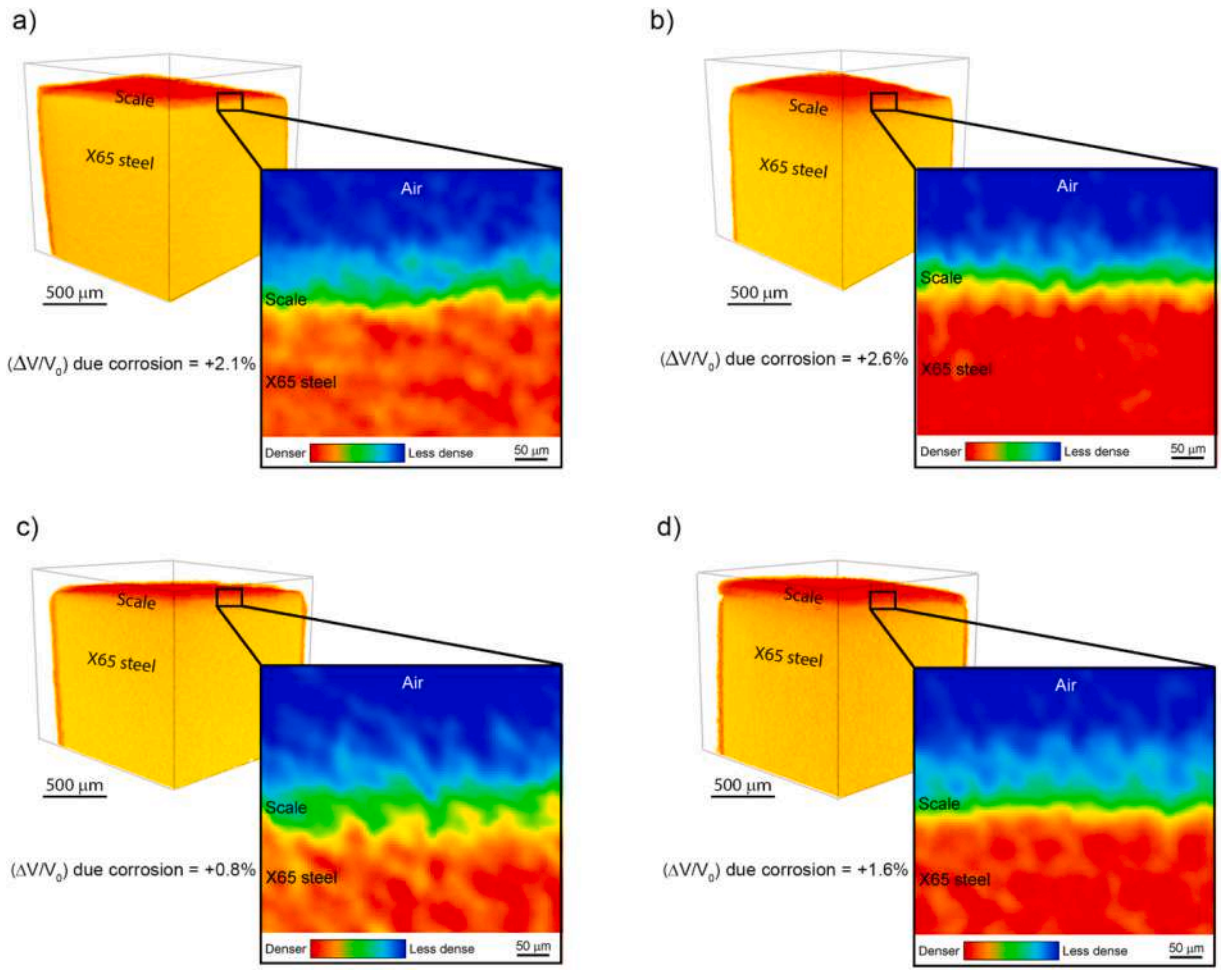

Fig. 7. X-ray MCT images of the selected areas of specimens after corrosion, cross-section density color maps, and total volume variation due corrosion. a) 7 d/brine; b) 15 d/brine; c) 7 d/NaCl; and d) 15 d/NaCl.

heterogeneity and porosity of the surface do not allow adjustment to an ideal capacitive response. A Warburg impedance element (W) was also included, representing an ion-diffusion-controlled process through the layers.

Scales grown for 7 d in brine or NaCl showed little difference in performance, although the R_{inner} and R_{ct} values were higher for scales composed of $FeCO_3$ formed in NaCl. In contrast, scale grown for 15 d in NaCl presented much higher resistances (R_{outer} and R_{inner}) and lower Warburg (W) impedance than the scales grown for 7 d. Therefore, $FeCO_3$ scale formed for 15 d in NaCl has provided superior protection to steel substrates against corrosion than $Fe_{1-x}Ca_xCO_3$ scales. The lower R_{ct} value exhibited by both scales grown for 15 d can be attributed to the lower thicknesses of the inner layer with respect to those of 7 d scales, particularly for the inner layers. The EIS results are consistent with the results reported by Yue et al. [10], which demonstrated that the replacement of Fe lattice sites by Ca results in total volume expansion, weakening the bonds compared with pure $FeCO_3$. They showed that the change in energy of dissolution by losing Ca^{2+} ion (785.5 kcal/mol) is smaller compared with that of losing Fe^{2+} ion (832.0 kcal/mol), suggesting the degradation of corrosion products by preferential breaking of Ca—O bonds.

3.4. Mechanical and tribological properties of the scales

The scale hardness and elastic modulus presented in Fig. 12 show that there is a small variation in these properties regardless of the exposure time and the solution that the specimens were exposed. The scales formed for a longer period (15 d) presented higher hardness and elastic modulus, probably due to their greater compactness, as shown in Fig. 4. The average hardness and elastic modulus were slightly higher for scales grown in NaCl after 15 d. However, a large standard deviation was observed, which can be attributed to the scale inhomogeneity and presence of pores, as shown in in Fig. 4b and d. The results demonstrate an average elastic modulus ranging from approximately 68 to 83 GPa, which is comparable to the values reported by Gao et al. [25]. They obtained an elastic modulus for X65 steel of approximately 95 GPa for experimental corrosion conditions of 65 °C, PCO_2 ranging from 0.1 to 1 MPa, and 240 h of corrosion. Zhang et al. [24] obtained a higher elastic modulus for X65 steel, approximately 148 GPa, for experimental corrosion conditions of 50 °C, 9.5 MPa, and 7 d. The differences in the reported elastic modulus by the different studies can be attributed to the presence of defects, such as voids and cracks, differences in chemical compositions, and distinct degrees of compactness according to the environmental conditions of growth.

A preliminary set of wear tests was performed using a 2 N load and 10 min to verify the wear condition in both the corrosion product scales and the substrate. Fig. 13a shows the values for the COF as a function of time for scales grown for 15 d. Analysis of the curves indicates two distinct regions: an initial region where the COF increases quickly with time in a non-linear manner, and a region where the COF is almost constant, showing a quasi-linear relationship between the coefficient and time. Figs. 13b and c present the OM and SEM images of the wear scar for brine and NaCl solution, respectively. A detail of the border of the wear scar is shown in Fig. 13b. It can be observed, mainly in the OM

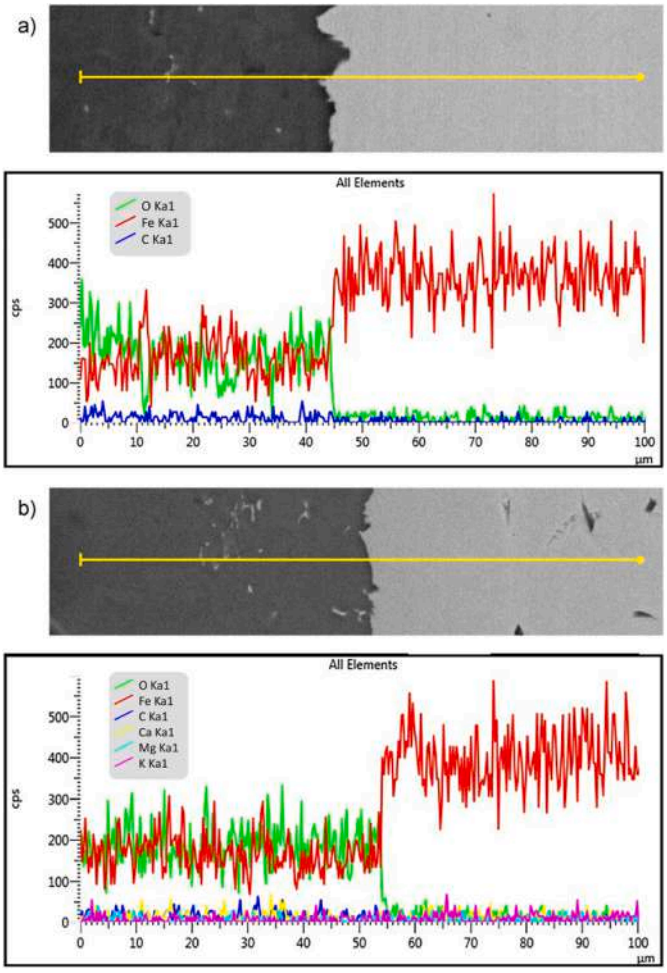

Fig. 8. SEM images and respective EDS line scan analysis for cross sections of the corrosion product scales formed on X65 steel surface at 40 °C and 15 MPa in different media: a) 15 d/brine and b) 15 d/NaCl.

Table 4
Cation quantifications (mg/L) obtained using ICP/EOS in solutions before and after corrosion.

Solution/ condition	Fe^{2+}	Ca^{2+}	K^{+}	Mg^{2+}
7 d Brine Before corrosion	0.07914 ± 0.00011	87.8 ± 1.6	496 ± 6	23.54 ± 0.60
7 d Brine After corrosion	162.72 ± 0.62	72.9 ± 1.0	507 ± 11	25.74 ± 0.51
15 d Brine Before corrosion	0.02638 ± 0.00033	97.2 ± 2.0	507 ± 12	25.68 ± 0.62
15 d Brine After corrosion	111.47 ± 0.33	67.4 ± 0.3	493 ± 11	25.60 ± 0.48
7 d NaCl Before corrosion	0.06069 ± 0.00054	–	–	–
7 d NaCl After corrosion	175 ± 1.1	–	–	–
15 d NaCl Before corrosion	0.03794 ± 0.00022	–	–	–
15 d NaCl After corrosion	64.11 ± 0.28	–	–	–

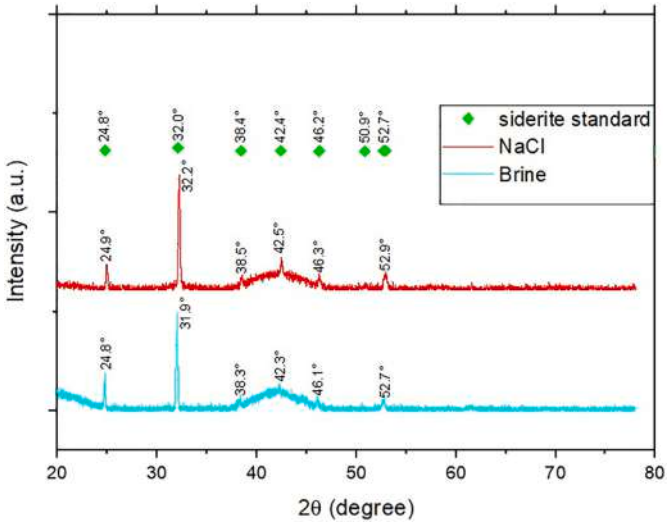

Fig. 9. XRD patterns of scales formed on API X65 steel surface at 40 °C and 15 MPa in different media for 7 d.

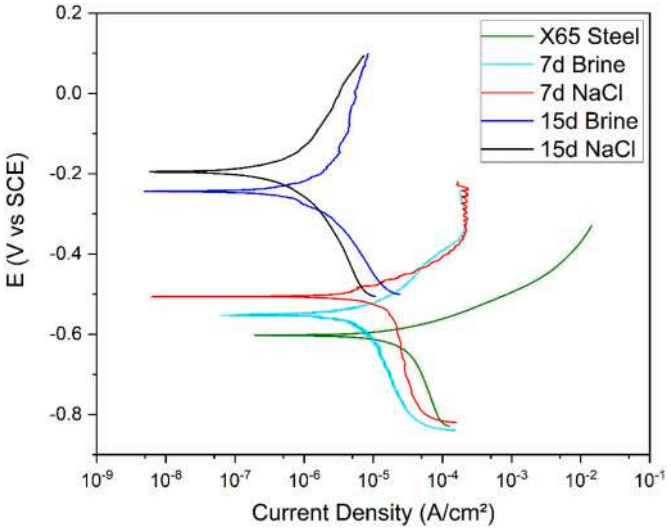

Fig. 10. Polarization curves of corrosion product scales formed on X65 steel surface at 40 °C and 15 MPa in different media and immersion period in a 0.1 M Na_2SO_4 solution.

Table 5
Electrochemical parameters obtained by PP technique for corrosion product scales in 0.1 M Na_2SO_4 solution.

Scale/condition	E_{corr} (mV)	i_{corr} (A/cm^2)	R_p (Ω.cm^2)
X65 Steel	−602	1.9×10^{-4}	8.9×10^{2}
7 d Brine	−555	1.3×10^{-5}	4.8×10^{3}
7 d NaCl	−504	3.1×10^{-5}	2.2×10^{3}
15 d Brine	−240	3.6×10^{-6}	2.8×10^{4}
15 d NaCl	−192	1.4×10^{-6}	6.4×10^{4}

images, that wear occurred in the scales (orange areas) and in a lower degree in the steel (white areas).

Fig. 14a presents the COF as a function of time with 2 and 8 N applied loads and scales grown for 15 d in brine and NaCl when the test duration was increased from 10 to 30 min. Under the application of a lower load (2 N), an initial transient friction regime was observed in the first 10 min, after which a steady-state behavior was attained. The results for 2 N

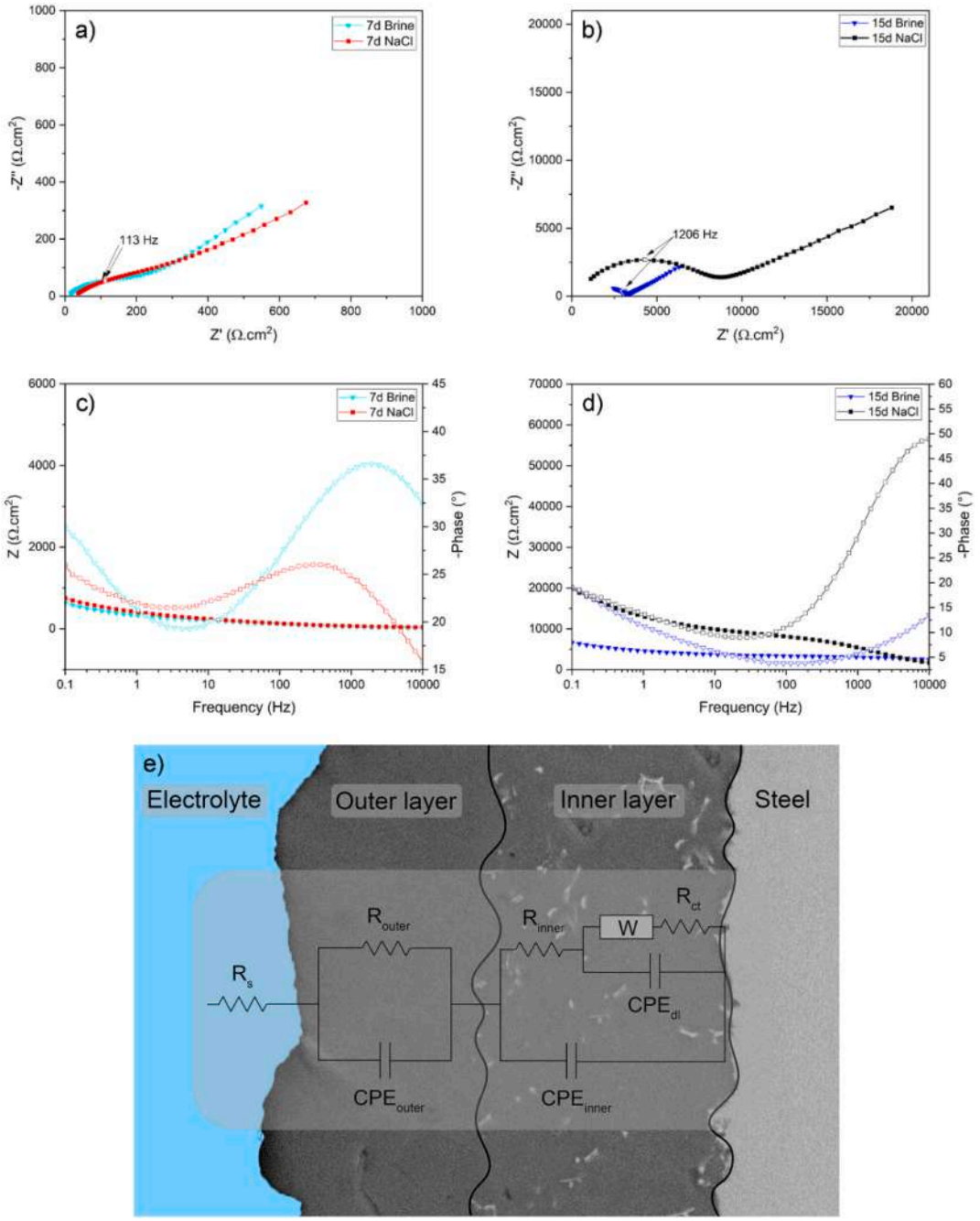

Fig. 11. a) and b) Nyquist plots; c) and d) Bode plots; e) EECs of corrosion product scales formed on X65 steel surface at 40 °C and 15 MPa with different media and exposure times in 0.1 M Na_2SO_4 solution.

Table 6
Electrochemical parameters obtained by EIS technique of corrosion product scales in 0.1 M Na_2SO_4.

Condition	χ^2	CPE_{outer}		R_{outer} ($\Omega.cm^2$)	CPE_{inner}		R_{inner} ($\Omega.cm^2$)	CPE_{dl} ($F\ cm^{-2}\ s^{n-1}$)		R_{ct} ($\Omega.cm^2$)	W ($\Omega.cm^2$)
		Yo ($F.cm^{-2}.s^{n-1}$)	n		Yo ($F.cm^{-2}.s^{n-1}$)	n		Yo ($F.cm^{-2}.s^{n-1}$)	n		
7 d brine	1.4×10^{-5}	1.5×10^{-4}	0.6	1.4×10^{2}	3.3×10^{-11}	0.8	7.3	2.3×10^{-4}	0.7	4.2	2.9×10^{2}
7 d NaCl	4.8×10^{-5}	1.2×10^{-4}	0.5	1.1×10^{2}	4.9×10^{-21}	0.9	27.5	2.1×10^{-4}	0.7	29.1	3.7×10^{2}
15 d brine	2.3×10^{-5}	4.0×10^{-7}	0.6	2.8×10^{3}	2.4×10^{-4}	0.6	6.6×10^{3}	1.0×10^{-20}	0.6	1.7×10^{-3}	22.0
15 d NaCl	2.3×10^{-5}	1.5×10^{-7}	0.7	6.9×10^{3}	8.4×10^{-5}	0.3	1.8×10^{5}	3.1×10^{-17}	0.5	0.2	3.1×10^{-4}

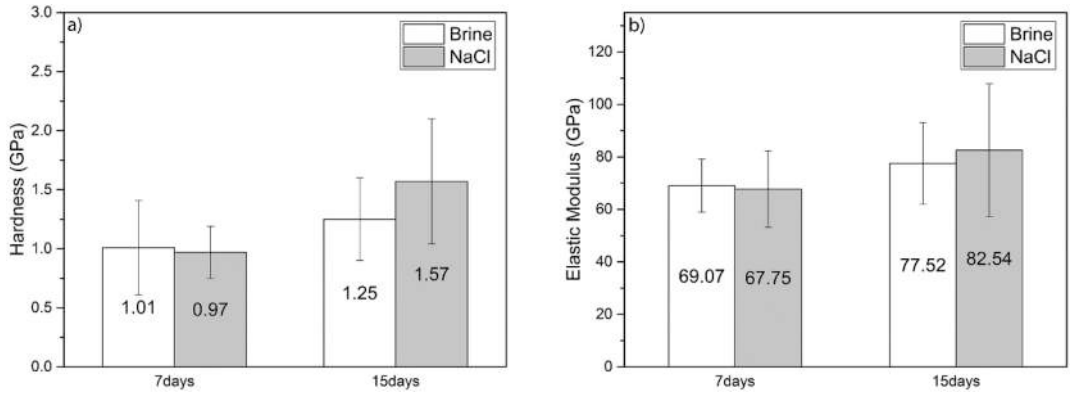

Fig. 12. (a) Hardness and (b) elastic modulus of the corrosion product scales formed on X65 steel surface at 40 °C and 15 MPa in different media and durations.

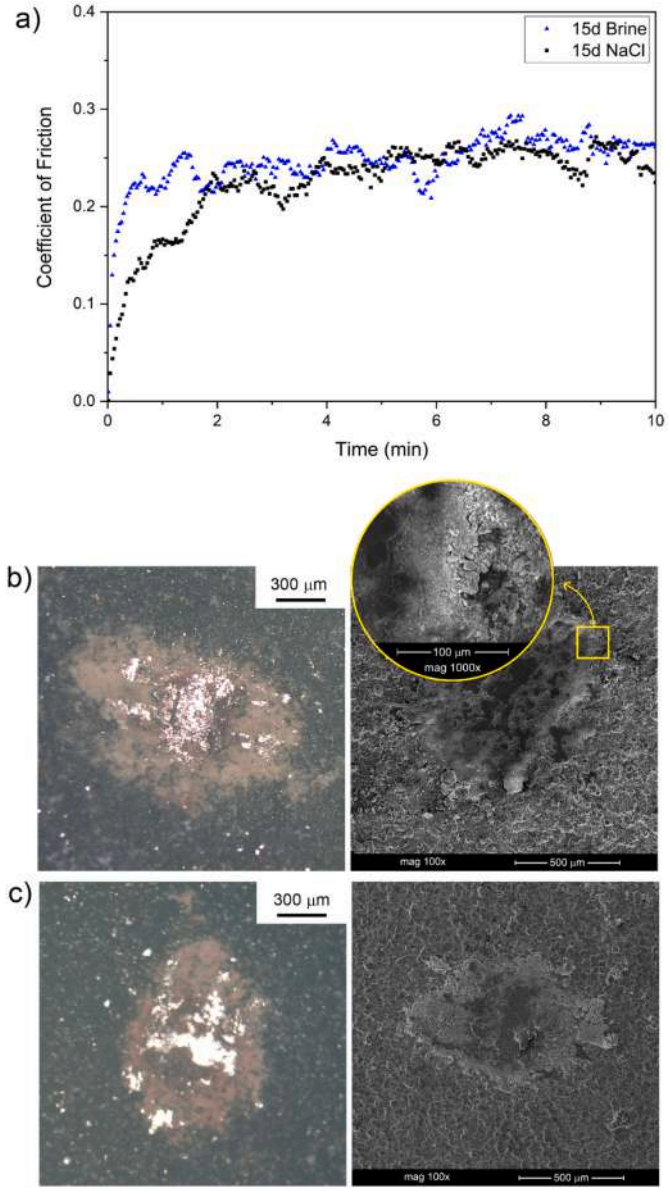

Fig. 13. a) COF as a function of time with 2 N applied load and 10 min test duration in different media for 15 d; OM (left column) and SEM (right column) images of the scar wear in: b) brine; c) NaCl solution.

load were practically identical to those observed in the preliminary tests for 10 min. When the load is increased (8 N), a steady state is achieved after approximately 5 min. The initial transient regime probably occurs owing to the surface roughness, which induces the fragmentation and extraction of material from the surface by abrasion, as detailed in Fig. 13b. The scales exhibited similar wear responses in terms of the COF, considering the same applied load and in the steady-state regime. However, the scales grown in brine exhibited a slightly higher COF at the beginning of the wear test under both applied loads. This can be attributed to the formation of complex carbonate with Ca substitution in the $FeCO_3$ lattice that can induce stress owing to the larger Ca atomic ratio compressing the Fe—O bonds [10], and, consequently, cannot initially be removed.

After measuring the wear scars of the scales formed after 15 d in both media under an applied load of 2 N for 30 min (Figs. 14b and c), the wear volume was calculated by considering the volume of a semi-ellipsoid. The removed material volume was almost the same for both media ($\sim 0.88 \times 10^{-2}$ mm^3). When the applied load was increased to 8 N (Figs. 14d and e), a discrete difference in the removed material volume was observed (1.66×10^{-2} mm^3 for brine and 1.42×10^{-2} mm^3 for NaCl solution). Although the thicknesses of the scales formed in the NaCl solution and brine were practically the same, the hardness of the scale formed in brine was lower than that in the NaCl solution, which could lead to more severe wear in the brine condition. Usually, a rougher surface results in more severe wear and a higher COF. The surface roughness and morphology of the scales showed that the NaCl solution yielded a smooth surface with thinner crystals, whereas brine resulted in a rough surface with coarser crystals. In addition, the chemical composition of the scales may influence their wear response. Scales formed in NaCl solution were composed of $FeCO_3$, while those formed in brine were composed of $Fe_xCa_{1-x}CO_3$. When a longer test period and same load for both scales were used, difference lower than 0.01 mm^3 in the removed volumes was observed. This can be related to that the wear resistance of the inner layer is better than that of the outer layer. The inner layer contained a mix structure of a finer and denser distribution of carbides and carbonates, which provided greater wear resistance and protected the substrate, while the outer layer is composed of only carbonates with lower density and coarser crystals. These results agree with those of Lin et al. [27], who evaluated wear in a water–sand double-phase medium using a self-assembled wear device and observed high wear resistance for the inner layer.

The wear rate for each condition was determined with the removed material volume, as shown in Fig. 15. This behavior can be attributed to the particular properties of the $Fe_xCa_{1-x}CO_3$ scale, which presented decreased density and hardness. However, a better understanding of the wear responses of corrosion product scales formed in CO2 supercritical pressure media needs to be achieved.

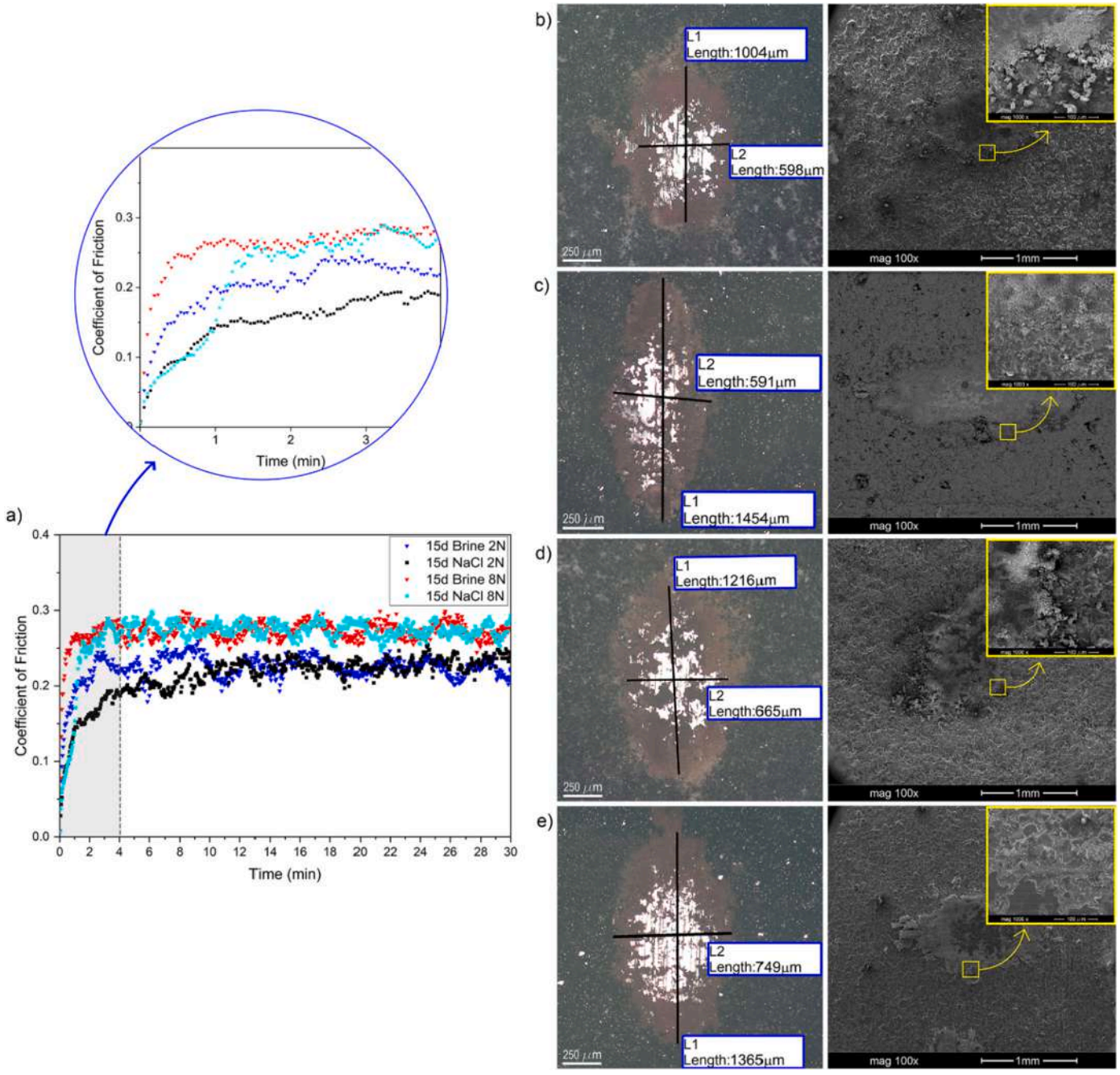

Fig. 14. a) COF as a function of time with 2 and 8 N applied loads and 30 min test duration in different media for 15 d; scar wear for different wear conditions: b) Brine, 2 N; c) NaCl, 2 N; d) Brine, 8 N; e) NaCl, 8 N. Left column: OM images; right column: SEM images.

3.5. General corrosion rates

Fig. 16 shows the general corrosion rates calculated using mass loss. The scales grown in brine have shown higher corrosion rate during corrosion durations (7 and 15 d) as the results of previous reported [15,18,34,35]. This behavior suggests that the dissolution of corrosion products scales is easier in $Fe_xCa_{1-x}CO_3$. However, the corrosion rate has decreased significantly from 7 to 15 d for both media. For scales grown in NaCl, the average corrosion rate has decreased from 1.402 to 0.659 mm/y corresponding to a reduction of 53 %, while for the scales grown in brine, the average corrosion rate has decreased from 1.726 to 1.129 mm/y equivalent a decrease of approximately 35 %. These results confirm that the scales composed of $FeCO_3$ are more protective to steel than $Fe_xCa_{1-x}CO_3$.

4. Conclusions

From the experimental results attained the following conclusions can be drawn:

- In the presence of NaCl, the scale formed consisted of $FeCO_3$, whereas in brine, the scale was a mixed carbonate ($Fe_xCa_{1-x}CO_3$).
- All the scales exhibited a two-layer structure. The inner layer contained carbonate and carbide, whereas the outer layer contained only carbonate. The inner layer was denser than the outer layer, as demonstrated in the results on the X-ray MCT analysis.
- The PP and EIS results have shown that the $FeCO_3$ scales demonstrate higher resistance to the mass transfer of corrosive species than

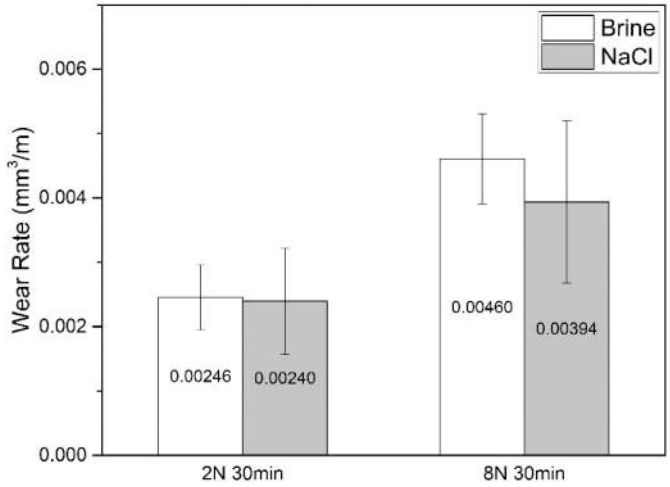

Fig. 15. Wear rate of scales for different wear conditions during 30 min test duration.

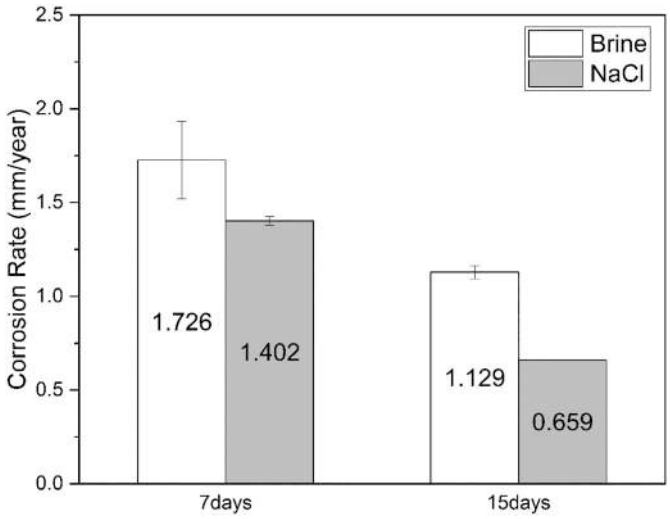

Fig. 16. Corrosion rate obtained after mass loss tests for different media and exposure times.

$Fe_xCa_{1-x}CO_3$. The presence of Ca has favored the scale dissolution, and the efficiency protection is decreased.

– $FeCO_3$ scales demonstrated enhanced protection capability of steel substrate against CO_2-corrosion, and improved mechanical and tribological properties compared to those with $Fe_xCa_{1-x}CO_3$. Scales formed for 15 d exhibited superior properties compared with those grown for 7 d.

CRediT authorship contribution statement

Katryanne Rohana Georg Bacca: Conceptualization, Methodology, Validation, Formal analysis, Investigation, Data Curation, Writing - Original Draft, Writing - Review & Editing, Visualization.

Natália Feijó Lopes: Conceptualization, Methodology, Validation, Formal analysis, Investigation, Data Curation, Writing - Original Draft, Writing - Review & Editing, Visualization.

Giovanni dos Santos Batista: Conceptualization, Methodology, Validation, Formal analysis, Investigation, Data Curation, Writing - Original Draft, Writing - Review & Editing, Visualization.

Carlos Alexandre dos Santos: Conceptualization; Methodology, Validation, Formal analysis, Writing - Original Draft, Writing - Review & Editing.

Eleani Maria da Costa: Conceptualization; Methodology, Validation, Formal analysis, Writing - Original Draft, Writing - Review & Editing, Supervision.

Data availability statement

Research data are not shared.

Declaration of competing interest

The authors declare that they have no known competing financial interests or personal relationships that could have appeared to influence the work reported in this paper.

Data availability

Data will be made available on request.

Acknowledgements

The authors acknowledge the support provided by the Brazilian Research Council (CNPq), Institute of Petroleum and Natural Resources (IPR) of PUCRS and Materials and Nanosciences Laboratory (LMN). This study was financed in part by the Coordenação de Aperfeiçoamento de Pessoal de Nivel Superior, Brasil (CAPES), Finance Code 001.

References

[1] E. Bowman, G. Koch, J. Varney, N. Thompson, O. Moghissi, M. Gould, J. Payer, International measures of prevention, application, and economics of corrosion technologies study, NACEInt. (2016) 1–216.
[2] Y.T. Al-Janabi, An overview of corrosion in oil and gas industry: upstream, midstream, and downstream sectors, in: Corrosion Inhibitors in the Oil And Gas Industry, 2020, pp. 3–39, https://doi.org/10.1002/9783527822140.ch1.
[3] A.H. Alamri, Localized corrosion and mitigation approach of steel materials used in oil and gas pipelines – an overview, Eng. Fail. Anal. 116 (2020), 104735, https://doi.org/10.1016/j.engfailanal.2020.104735.
[4] M. Askari, M. Aliofkhazraei, R. Jafari, P. Hamghalam, A. Hajizadeh, Downhole corrosion inhibitors for oil and gas production – a review, Appl.Surf.Sci.Adv. 6 (2021), 100128, https://doi.org/10.1016/j.apsadv.2021.100128.
[5] R. Rizzo, S. Gupta, M. Rogowska, R. Ambat, Corrosion of carbon steel under CO2 conditions: effect of CaCO3 precipitation on the stability of the FeCO3 protective layer, Corros. Sci. 162 (2020), https://doi.org/10.1016/j.corsci.2019.108214.
[6] M. Javidi, R. Chamanfar, S. Bekhrad, Investigation on the efficiency of corrosion inhibitor in CO2 corrosion of carbon steel in the presence of iron carbonate scale, J. Nat.Gas Sci.Eng. 61 (2019) 197–205, https://doi.org/10.1016/j.jngse.2018.11.017.
[7] M.B. Kermani, A. Morshed, Carbon dioxide corrosion in oil and gas production - a compendium, Corrosion 59 (2003) 659–683, https://doi.org/10.5006/1.3277596.
[8] L.T. Popoola, A.S. Grema, G.K. Latinwo, B. Gutti, A.S. Balogun, Corrosion problems during oil and gas production and its mitigation, <sb:contribution><sb:title>Int. J. Ind.</sb:title></sb:contribution><sb:host><sb:issue><sb:series><sb:title>Chem.</sb:title></sb:series></sb:issue></sb:host> 4 (2013) 1–15, https://doi.org/10.1186/2228-5547-4-35.
[9] R.A. De Motte, R. Barker, D. Burkle, S.M. Vargas, A. Neville, The early stages of FeCO3 scale formation kinetics in CO2 corrosion, Mater. Chem. Phys. 216 (2018) 102–111, https://doi.org/10.1016/j.matchemphys.2018.04.077.
[10] X. Yue, L. Zhang, Y. Hua, Fundamental insights into the stabilisation and chemical degradation of the corrosion product scales, npj Mater.Degrad. 5 (2021), https://doi.org/10.1038/s41529-021-00152-x.
[11] X. Wang, L. Fan, K. Ding, L. Xu, W. Guo, J. Hou, T. Duan, Pitting corrosion of 2Cr13 stainless steel in deep-sea environment, J. Mater. Sci. Technol. 64 (2021) 187–194, https://doi.org/10.1016/j.jmst.2020.04.036.
[12] R. Barker, D. Burkle, T. Charpentier, H. Thompson, A. Neville, A review of iron carbonate (FeCO3) formation in the oil and gas industry, Corros. Sci. 142 (2018) 312–341, https://doi.org/10.1016/j.corsci.2018.07.021.
[13] J.L. Crolet, N. Thevenot, S. Nesic, Role of conductive corrosion products on the protectiveness of corrosion layers, in: NACE - International Corrosion Conference Series 1996-March, 1996, pp. 194–203.
[14] M. Gao, X. Pang, K. Gao, The growth mechanism of CO2 corrosion product films, Corros. Sci. 53 (2011) 557–568, https://doi.org/10.1016/j.corsci.2010.09.060.
[15] S.N. Esmaeely, D. Young, B. Brown, S. Nešić, Effect of incorporation of calcium into iron carbonate protective layers in CO2 corrosion of mild steel, Corrosion 73 (2017) 238–246, https://doi.org/10.5006/2261.
[16] Y. Hua, S. Xu, Y. Wang, W. Taleb, J. Sun, L. Zhang, R. Barker, A. Neville, The formation of FeCO3 and Fe3O4 on carbon steel and their protective capabilities

against CO2 corrosion at elevated temperature and pressure, Corros. Sci. 157 (2019) 392–405, https://doi.org/10.1016/j.corsci.2019.06.016.
[17] L.M. Tavares, E.M. Da Costa, J.J.D.O. Andrade, R. Hubler, B. Huet, Effect of calcium carbonate on low carbon steel corrosion behavior in saline CO2 high pressure environments, Appl. Surf. Sci. 359 (2015) 143–152, https://doi.org/10.1016/j.apsusc.2015.10.075.
[18] C. Ding, K.-W. Gao, C. Chen, Effect of Ca2+ on CO2 corrosion properties of X65 pipeline steel, Int. J. Miner. Metall. Mater. 16 (2009) 661–666.
[19] B. Wang, L. Xu, G. Liu, M. Lu, Corrosion behavior and mechanism of 3Cr steel in CO2 environment with various Ca2+ concentration, Corros. Sci. 136 (2018) 210–220, https://doi.org/10.1016/j.corsci.2018.03.013.
[20] S.D. Zhu, G.S. Zhou, J. Miao, R. Cai, J.F. Wei, Mechanical properties of CO 2 corrosion scale formed at different temperatures and their relationship to corrosion rate, Corros.Eng.Sci.Technol. 47 (2012) 177–181, https://doi.org/10.1179/1743278211Y.0000000023.
[21] L. Wei, X. Pang, C. Liu, K. Gao, Formation mechanism and protective property of corrosion product scale on X70 steel under supercritical CO2 environment, Corros. Sci. 100 (2015) 404–420, https://doi.org/10.1016/j.corsci.2015.08.016.
[22] S.L. Wu, Z.D. Cui, G.X. Zhao, M.L. Yan, S.L. Zhu, X.J. Yang, EIS study of the surface film on the surface of carbon steel from supercritical carbon dioxide corrosion, Appl. Surf. Sci. 228 (2004) 17–25, https://doi.org/10.1016/j.apsusc.2003.12.025.
[23] R. Elgaddafi, R. Ahmed, S. Hassani, S. Shah, S.O. Osisanya, Corrosion of C110 carbon steel in high-pressure aqueous environment with mixed hydrocarbon and CO2 gas, J. Pet. Sci. Eng. 146 (2016) 777–787, https://doi.org/10.1016/j.petrol.2016.07.017.
[24] Y. Zhang, X. Pang, S. Qu, X. Li, K. Gao, Discussion of the CO2 corrosion mechanism between low partial pressure and supercritical condition, Corros. Sci. 59 (2012) 186–197, https://doi.org/10.1016/j.corsci.2012.03.006.
[25] K. Gao, F. Yu, X. Pang, G. Zhang, L. Qiao, W. Chu, M. Lu, Mechanical properties of CO2 corrosion product scales and their relationship to corrosion rates, Corros. Sci. 50 (2008) 2796–2803, https://doi.org/10.1016/j.corsci.2008.07.016.
[26] C. Prieto, H. Mansoori, B. Brown, M. Singer, D. Young, Application of scratch testing for the assessment of the adherent properties of scales and CO2 corrosion product layers and their relation to corrosion, Corros. Sci. 190 (2021), 109625, https://doi.org/10.1016/j.corsci.2021.109625.
[27] G. Lin, M. Zheng, Z. Bai, Y. Feng, Wear resistance of CO2 corrosion product scale formed at high temperature, <sb:contribution><sb:title>J. Iron Steel Res.</sb:title></sb:contribution><sb:host><sb:issue><sb:series><sb:title>Int.</sb:title></sb:series></sb:issue></sb:host> 13 (2006) 47–52, https://doi.org/10.1016/S1006-706X(06)60094-0.
[28] C.A. Schneider, W.S. Rasband, K.W. Eliceiri, NIH image to ImageJ: 25 years of image analysis, Nat. Methods 9 (2012) 671–675, https://doi.org/10.1038/nmeth.2089.
[29] S. Arzola, M.E. Palomar-Pardavé, J. Genesca, Effect of resistivity on the corrosion mechanism of mild steel in sodium sulfate solutions, J. Appl. Electrochem. 33 (2003) 1223–1231.
[30] O.A. Zambrano, J.J. Coronado, S.A. Rodríguez, Mechanical properties and phases determination of low carbon steel oxide scales formed at 1200°C in air, Surf. Coat. Technol. 282 (2015) 155–162, https://doi.org/10.1016/j.surfcoat.2015.10.028.
[31] ASTM, G1-03: Standard Practice for Preparing, Cleaning, And Evaluating Corrosion Test Specimens, 2017. West Conshohocken, PA.
[32] T. Tanupabrungsun, D. Young, B. Brown, S. Nesic, Construction and verification of Pourbaix diagrams for CO2 corrosion of mild steel valid up to 250°C, in: CORROSION 2012, Salt Lake City, 2012 https://onepetro.org/NACECORR/proceedings-abstract/CORR12/All-CORR12/NACE-2012-1418/120081.
[33] J. Han, J.W. Carey, J. Zhang, A coupled electrochemical-geochemical model of corrosion for mild steel in high-pressure CO2-saline environments, Int.J. Greenhouse Gas Control 5 (2011) 777–787, https://doi.org/10.1016/j.ijggc.2011.02.005.
[34] A. Shamsa, R. Barker, Y. Hua, E. Barmatov, T.L. Hughes, A. Neville, The role of Ca2+ ions on Ca/Fe carbonate products on X65 carbon steel in CO2 corrosion environments at 80 and 150°C, Corros. Sci. 156 (2019) 58–70, https://doi.org/10.1016/j.corsci.2019.05.006.
[35] Amin Rezaee, Ali Mobaraki Nejad, Hamidreza Mansouri, Scaling and corrosion in oil production-how do they relate to each other? Int. J. Eng. Appl. Sci. 4 (2017) 1–4.